

# A green synthesis of carbon nanoparticles from honey and their use in real-time photoacoustic imaging

Lina Wu<sup>1,2,§</sup>, Xin Cai<sup>3,§</sup>, Kate Nelson<sup>4</sup>, Wenxin Xing<sup>3</sup>, Jun Xia<sup>3</sup>, Ruiying Zhang<sup>3</sup>, Allen J. Stacy<sup>1</sup>, Micah Luderer<sup>1</sup>, Gregory M. Lanza<sup>1</sup>, Lihong V. Wang<sup>3</sup> (✉), Baozhong Shen<sup>2</sup> (✉), and Dipanjan Pan<sup>1</sup> (✉)

<sup>1</sup> C-TRAIN and Division of Cardiology, Washington University School of Medicine, 4320 Forest Park Avenue, Saint Louis, MO 63108, USA

<sup>2</sup> Key Laboratory of Molecular Imaging in College of Heilongjiang Province, Department of Radiology, the 4th Affiliated Hospital of Harbin Medical University, Harbin, 150001, China

<sup>3</sup> Optical Imaging Laboratory, Department of Biomedical Engineering, Washington University in St. Louis, Campus Box 1097, One Brookings Drive, St. Louis, MO 63130, USA

<sup>4</sup> Nano Research Facility (NNIN-NSF), Washington University in St. Louis, St. Louis, MO 63130, USA

<sup>§</sup> These authors contributed equally to this work

**Received:** 11 February 2013

**Revised:** 14 March 2013

**Accepted:** 16 March 2013

© Tsinghua University Press  
and Springer-Verlag Berlin  
Heidelberg 2013

## KEYWORDS

carbon nanoparticle,  
honey,  
contrast agents,  
photoacoustic  
tomography,  
real-time imaging

## ABSTRACT

Imaging sentinel lymph nodes (SLN) could provide us with critical information about the progression of a cancerous disease. Real-time high-resolution intraoperative photoacoustic imaging (PAI) in conjunction with a near-infrared (NIR) probe may offer opportunities for the immediate imaging for direct identification and resection of SLN or collecting tissue samples. In this work a commercially amenable synthetic methodology is revealed for fabricating luminescent carbon nanoparticles with rapid clearance properties. A one-pot “green” technique is pursued, which involved rapid surface passivation of carbon nanoparticles with organic macromolecules (e.g., polysorbate, polyethyleneglycol) in solvent-free conditions. Interestingly, the naked carbon nanoparticles are derived for the first time, from commercial food grade honey. Surface coated particles are markedly smaller (~7 nm) than previously explored particles (gold, single-walled carbon nanotubes, copper) for SLN imaging. The results indicate an exceptionally rapid signal enhancement (~2 min) of the SLN. Owing to their strong optical absorption in the NIR region, tiny size and rapid lymphatic transport, this platform offers great potential for faster resection of SLN and may lower complications caused in axillary investigation by mismarking with dyes or low-resolution imaging techniques.

## 1 Introduction

Photoacoustic imaging (PAI) elegantly unites light and sound to achieve a depth of vision that is not typically

offered by conventional optical imaging techniques [1–6]. The potential of PAI in molecular imaging in combination with suitably targeted contrast agents has been demonstrated. Among the most exciting

Address correspondence to Dipanjan Pan, dipanjan@wustl.edu; Baozhong Shen, shenbzh@vip.sina.com; Lihong V. Wang, lhwang@seas.wustl.edu

advances is the ability of PAI to quantify the levels of vascularization and oxygen saturation in tumors, and to detect nascent angiogenic sprouts [7–13]. Sentinel lymph node biopsy (SNB) exemplifies another important area where PAI offers great potential over current imaging practice [14, 15]. Sentinel lymph nodes (SLN) are the nodes nearest a tumor (e.g., breast or prostate tumor) to which cancerous cells would migrate at an early stage of the disease. In the clinic today, during a SNB, a radioactive agent or a dye (methylene blue) is injected to track the flow of these agents to the first draining lymph node to be filtered. Highly dependent on the surgical skill of the physician, this procedure offers limited success, giving only a rough estimate of the node's location. To further locate the node, the surgeon must reveal the area in an invasive way to follow the dye visually to the SLN. Furthermore, the positive predictive value of this procedure is less than ten percent for the patients undergoing this procedure and approximately five percent endure side effects (such as lymph edema or numbness). Real-time high-resolution intraoperative PAI imaging could facilitate direct assessment of the SLN location within the axilla independent of the patient position on the Operating Room (OR) table [16–20]. With immediate imaging, the resection of SLN or collecting tissue samples would be faster and minimize complications. To the best of our knowledge, the possibilities for real-time intraoperative SLN imaging with an exogenous contrast agent is mostly unexplored and thus the focus of the present work.

Photoacoustic SLN mapping has been demonstrated previously by us and other groups using various contrast agents, such as organic dyes [21], gold nanoparticles (Au NPs) [4, 22, 23], copper neodecanoate nanoparticles (Cu NPs) [14], single-walled carbon nanotubes (SWNT) and others [24–27]. Although all these contrast agents have shown potential for Photoacoustics (PA) SLN mapping with a depth capability of several centimeters, satisfactory spatial resolution and prospects for pre-clinical use, there are some limitations in their application. Organic dyes are widely used in clinics because of their ready availability and low cost. However, the dye molecules (e.g., methylene blue) are rather small (<2 nm), and thus they can easily transport into the echelon lymph nodes, causing a high possibility of producing false

positives [28]. Furthermore, they easily cause skin staining that may lead to irritation. Au NPs of different sizes and morphologies have been widely explored due to their strong optical absorption in the near-infrared (NIR) spectral region, which helps to achieve deep penetration. Au NPs can easily be bioconjugated with various types of ligands to target specific receptors [29], potentially eliminating the need for invasive axillary staging procedures in addition to providing noninvasive SLN mapping. Gold nanobeacons (GNB) have been explored for targeted PA imaging application for cancerous (e.g., angiogenesis) and cardiovascular (e.g., fibrin) biomarkers [4]. The signal strength of GNBs shows a PA spectrum over wavelengths from 721 to 823 nm. Within this range, GNB produced 15 times stronger signal than rat blood at a gold concentration of 1,080  $\mu\text{g/g}$  of the 20% colloid suspension. However, the optical properties of gold are highly dependent on expensive and complicated surface chemistries and their clinical use is discouraged by the unpredictable high cost. The intrinsic optical properties of copper have been recently exploited to generate high intensity photoacoustic signals in the low NIR region [14]. Copper-based nanoparticles could potentially provide an innovative, inexpensive, and commercially viable approach. Despite their high stability in suspension and *in vivo*, copper is known to pose neurotoxicity [30]. SWNTs are inexpensive but the safety of these materials is still an ongoing debate [31, 32]. The PA signal strength of SWNTs has been reported to be  $\sim 3.4$  times of the blood signal at 1,064 nm (at 1 mg/mL) and  $\sim 3.5$  times the blood signal at 764 nm (at 0.25 mg/mL). We have recently demonstrated the effectiveness of a NIR cyanine dye-loaded polymeric particle (ca. 20 nm) for real-time, high-resolution intraoperative photoacoustic imaging to facilitate direct assessment of the SLN [33]. Clearly, a more clinically translatable approach is warranted addressing healthcare cost, patient inconvenience, and small risks involved with preoperative labeling. We anticipate that a particle less than ten nanometers in size with stable optical properties will essentially be the same size as small proteins (e.g., albumin) and have the most rapid lymphatic transit time, yet be bulky enough for retention and phagocytosis by draining cortical macrophages. These particles can be tracked by real-time PAI and may assist direct evaluation of the SLN location to

help with the resection.

Towards this aim, we report a solvent free “green synthesis” of carbon nanoparticles (ca. 7 nm), whose surface is passivated with organic macromolecules. In the past, a wide range of carbon particles has been prepared by thermal decomposition, laser ablation or other methods [34–37], and some of them have shown great potential in biomedicine [38–42]. However, most of the existing techniques for producing a stable, aqueous suspension of carbon nanoparticle are cumbersome and may not be suitable for large scale commercial manufacturing. In contrast, the present technique is simple and can be performed under solvent-free conditions using a domestic microwave. Our hypothesis is that these luminescent carbon nanoparticles (OCN) will act as a sensitive exogenous contrast agents for PAI, exhibit high stability and by virtue of their tiny size (< 10 nm), facile lymphatic transport will be observed.

## 2 Experimental section

### 2.1 General experimental procedure

Unless otherwise listed, all solvents and reagents were purchased from Aldrich Chemical Co. (St. Louis, MO) and used as received. Argon (ultra high purity: UHP, 99.99%) was used for storage of materials. The Spectra/Por membrane (Cellulose MWCO: 20,000 Da) used for dialysis was obtained from Spectrum Medical Industries, Inc. (Laguna Hills, CA).

### 2.2 Synthesis of luminescent carbon nanoparticles from honey

Commercial food grade honey (Great Value™ Clover Honey 1 wt.%; batch composition—fructose: 38%, glucose: 31%, maltose: 7.1%, sucrose: 1.3% higher sugars: 1.5%, water: 17.2%) was suspended with an organic macromolecular passivating agent (8 wt.%; (x)-sorbitan mono-9-octadecenoate poly(oxy- 1,2-ethanediyl) or polyethyleneglycol (with a molecular weight (MW) of 400 Da, PEG<sub>400</sub>)), purged with argon and heated in a domestic microwave oven for 30 min. Microwave power was set at 1,200 W with an output power of 50%. The product visually changed from light yellow to dark brown to black. The as-synthesized nanoparticles were purified by repeated centrifugation in water.

### 2.3 Dynamic light scattering measurements

Hydrodynamic diameter distribution and distribution averages for the OCN in aqueous solutions were determined by dynamic light scattering. Hydrodynamic diameters were determined using a Brookhaven Instrument Co. (Holtsville, NY) Model Zeta Plus particle size analyzer. Nanoparticles were dialyzed into water prior to analysis. Scattered light was collected at a fixed angle of 90°. A photomultiplier aperture of 400 mm was used, and the incident laser power was adjusted to obtain a photon counting rate between 200 and 300 kcps. Only measurements for which the measured and calculated baselines of the intensity autocorrelation function agreed to within +0.1% were used to calculate nanoparticle hydrodynamic diameter values. All determinations were made in multiples of five consecutive measurements.

### 2.4 Electrophoretic potential measurements (zeta potential)

Zeta potential ( $\zeta$ ) values for the OCN were determined with a Brookhaven Instrument Co. (Holtsville, NY) model Zeta Plus zeta potential analyzer. Measurements were made following dialysis (MWCO 20 kDa dialysis tubing, Spectrum Laboratories, Rancho Dominguez, CA) of nanoparticle suspensions into water. Data were acquired in the phase analysis light scattering (PALS) mode following solution equilibration at 25 °C. Calculation of  $\zeta$  from the measured nanoparticle electrophoretic mobility ( $\mu$ ) employed the Smoluchowski equation:  $\mu = \varepsilon\zeta/\eta$ , where  $\varepsilon$  and  $\eta$  are the dielectric constant and the absolute viscosity of the medium, respectively. Measurements of  $\zeta$  were reproducible to within  $\pm 4$  mV of the mean value given by 16 determinations of 10 data accumulations.

### 2.5 Raman spectroscopy

Raman measurements were performed with a Renishaw InVia spectrometer using the 532 nm wavelength of an Ar<sup>+</sup> laser. The instrument was calibrated using an internal silicon standard (521 cm<sup>-1</sup>). The spectrum was obtained using a dynamic scan for 5 accumulations at 1 s exposure time each at 10% laser intensity (23 mW). The Raman spectrum of pure Si was subtracted from the spectrum of collected carbon nanoparticles.

## 2.6 NMR spectrometry

$^1\text{H}$  NMR spectra were measured with a Varian Unity INOVA 600 (Varian Assoc., Palo Alto, CA) spectrometer at 25 °C in  $\text{D}_2\text{O}$ .

## 2.7 SEM imaging and energy-dispersive X-ray spectroscopy (EDX) analysis

The samples on Si wafers were imaged using a Nova NanoSEM 230 EDAX Genesis in high vacuum mode at 10 kV and at a working distance of 5 mm. Samples were prepared as follows: One drop of OCN suspension in nanopure water was deposited on a piece of clean Si wafer (the Si wafer was rinsed and sonicated in nanopure water, ethanol and acetone respectively). After 1 min, excess liquid was removed by touching the edge of the liquid bead using a piece of filter paper. The sample was allowed to air dry for 1 h before sputter coating, and then was sputter coated with Au–Pd for 15 seconds at 25 mA.

EDX was performed using EDAX Genesis at 10 kV and a working distance of 5 mm. Single point analysis was used to collect spectrum from the nano particles. Background noise was subtracted from the spectra and standardless quantitative analysis results were obtained using Genesis software with automatic corrections for atomic number, absorption, and fluorescence.

## 2.8 Fourier transform infrared (FT–IR) spectroscopy

A Thermo Nicolet Nexus470 FT–IR with SmartPerformer–ATR sampler with a Ge crystal was used for FT–IR measurements. The system was purged with dry air during collection of the baseline spectrum (air) and during the analysis. The Ge crystal was covered with the carbon nanoparticle sample and 12 psi of pressure was applied to the sample during the analysis.

## 2.9 Transmission electron microscopy (TEM) measurements

A 10  $\mu\text{L}$  aliquot of the diluted OCN stock solution was placed on a 400 mesh copper grid. After 1 min, excess fluid was removed by a piece of filter paper. Samples were viewed using a JEOL 1200EX electron microscope operating at 80 kV. High-resolution samples were viewed and analyzed with a Philips Tecnai F20

field emission gun electron microscope operating at 200 kV.

## 2.10 Atomic force microscopy (AFM) measurements

A Digital Instruments Dimension 3000 series AFM and standard Veeco tapping mode silicon probes with platinum–iridium (PtIr) coating were used for scanning the samples. Typically, aqueous suspensions of carbon nanoparticle samples were dried in a class 10,000-clean room on a clean glass slide for 3 h. Once dried, samples were placed on the AFM and scanned. Pertinent scanning parameters were as follows: Resonant frequency (probe): 60–80 kHz; Example of tip velocity: (4  $\mu\text{m/s}$  for 2  $\mu\text{m}$ ), (15  $\mu\text{m/s}$  for 5  $\mu\text{m}$ ), (30  $\mu\text{m/s}$  for 10  $\mu\text{m}$ ). Aspect ratio: 1:1; Resolution: 512 samples/line, 256 lines.

## 2.11 Blood-smear experiment

A single blood smear was prepared by drop depositing fresh mouse blood on the slide (near the end). The blood drop was spread by using a second slide (“spreader”), placing the spreader at a 45° angle and backing into the drop of blood. The spreader holds the drop and spreads it by capillary action along its edge. The smear was allowed to air dry for 1 min and a cover-slip added before being placed directly on the microscope and observed under 20x and 40x magnifications. A ratio of 1:4 OCN and mouse blood was used for preparation of the smear. The smear was prepared after incubation for 20 min.

## 2.12 Animal research studies

Guidelines on the care and the use of laboratory animals at Washington University in St. Louis were followed for all animal experiments. For SLN imaging, adult nude mice were anesthetized with a mixture of ketamine (85 mg/kg) and xylazine (15 mg/kg) and maintained on 0.75% isoflurane delivered through a calibrated vaporizer. OCN were administered (1 mL/kg) intradermally into the forepaw of the rat. PA images were acquired before and after the administration of the nanoparticle. During image acquisition, anesthesia was maintained with isoflurane (1 L/min oxygen and 0.75% isoflurane, Euthanex Corp.) and vital signs and pulse oximetry (NONIN Medical

INC., 8,600 V) were monitored continuously. Hydration was maintained by infusing 8 mL of 0.9% saline subcutaneously into the animal at a distal site as needed. After image acquisition, the animals were euthanized by pentobarbital overdose.

### 2.13 Photoacoustic spectroscopy and imaging system

In the PA system, the sample is irradiated by a short-pulsed laser beam, and then the absorbed light is partially converted to heat, subsequently inducing an acoustic wave via thermoelastic expansion. The acoustic wave is collected by the ultrasound transducers and is used to form an image by the computer.

The system is an updated version described in our previous publication [20]. The schematic is shown in Fig. S1 (in the Electronic Supplementary Material (ESM)). Three light sources are used: (1) Tunable OPO laser (450–685 nm, Vibrant (HE) 355 I, OPOTEK); pulse width 5 ns, pulse repetition rate 10 Hz; (2) Tunable Ti:sapphire laser (730–850 nm, LT-2211A, LOTIS TII) pumped by a Q-switched Nd:YAG (LS-2137/2, LOTIS TII); pulse width < 15 ns, pulse repetition rate 10 Hz. (3) Tunable dye laser (Emission dye: DCM, 590–685 nm, Cobra, Sirah) pumped by a Nd:YLF laser (INNOSLAB, EdgeWave); pulse width 7 ns, pulse repetition rate up to 5 kHz. In this work, the first two sources were used for preliminary spectroscopic study and the third source was used for *in vivo* nude mouse experiments. The emitted light was coupled into a multimode fiber (M30L02, Thorlabs), passed through a conical lens, and then weakly focused by an optical condenser into the sample. Then the generated ultrasound signal was collected by the acoustic lens, which is in confocal arrangement with focused laser beam, and received by a 20 MHz ultrasound transducer. The electrical signal from the transducer was amplified, digitized by the Data acquisition (DAQ) and converted to a one-dimensional depth-resolved image (“A-lines”) by the computer. By raster-scanning the entire area, a three-dimensional image is acquired. A field of view (FOV) of 12 mm × 10 mm can be acquired within ~1 min. The lateral and axial resolutions of the system are 80 μm and 30 μm, respectively. The pulse energy at the skin surface is ~5 mJ/cm<sup>2</sup>, which is well below the limit regulated by the American National Standards Institute standards (ANSI Z136.1).

### 2.14 *In vivo* biodistribution experiment

Biodistributions of OCN were studied at 2 h and 24 h post-I.V. and post-I.D. injection, respectively. Animals (*n* = 5) were sacrificed, and their major organs (i.e., liver, spleen, kidneys, lung, spleen, lymph nodes) were excised and imaged *ex vivo* with a Xenogen IVIS<sup>TM</sup> spectrum imaging system. The identical settings (excitation, 535 nm; emission, 580 nm; exposure time, 0.5 s; binning factor, 8; *f* value, 2; FOV, 12.9) were used for all imaging acquisitions. Fluorescence emission was normalized to photons per second per centimeter squared per steradian (p/sec/cm<sup>2</sup>/sr), and the influence of backgrounds was deducted.

## 3 Results and discussion

Honey is a natural sweetener, produced by bees using nectar from flowers by a process of regurgitation and evaporation. It is a complex mixture of carbohydrates, water, dietary fiber and fat. A typical commercial food grade honey is predominantly a mixture of monosaccharides and higher sugars, which can act as an excellent precursor material for synthesizing carbon nanoparticles. The use of honey has never been explored to derive nanoparticles in the literature. In a typical synthesis, commercial food grade honey was suspended with an organic macromolecular passivating agent (8 wt.%; (x)-sorbitan mono-9-octadecenoate poly(oxy-1,2-ethanediyl) or PEG<sub>400</sub>), purged with argon and heated in a domestic microwave oven for 10–30 min (Fig. 1(a)). Two different organic macromolecules were chosen to investigate the effect of surface passivation and our initial results indicate that similar optical properties were obtained from both polysorbate and PEG<sub>400</sub> coated OCN. PEG-coated OCN was considered for further *in vivo* investigation. As-synthesized OCN particles are soluble in solvents with a wide range of polarities (Fig. 1(b)). The ratio of the honey and passivating agent was varied from 1:1 to 1:8. The formation of carbon particles was observed even in the presence of lower amounts (< 8 wt.%) of passivating agent. However, their dispersion in solvents was relatively troublesome presumably due to the incomplete surface coating (Fig. 1(c) (left)). In aqueous suspension, the polysorbate-coated OCN particles and

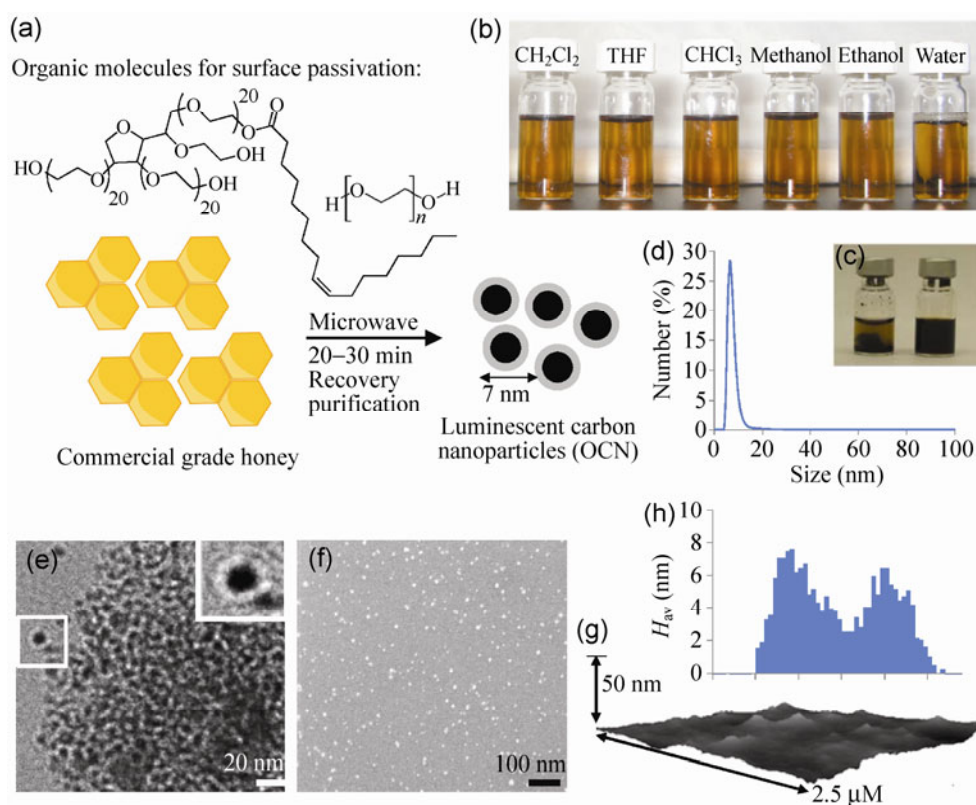


**Figure 1** Preparation of luminescent carbon nanoparticles: (a) Commercial grade honey (neat), passivating agent (x)-sorbitan mono-9-octadecenoate poly(oxy-1,2-ethanediyl) or polyethyleneglycol (MW = 400 Da), microwave, 20–30 min; isolation of particles; (b) solubility of OCN in a wide range of solvents; (c) optical picture showing a stable suspension of evenly coated highly concentrated OCN (33 wt./vol.%) after 7 days (right) vs. agglomerated particles in the bottom for an unevenly coated OCN (left); (d) number-averaged particle diameter from dynamic light scattering of as-synthesized OCN dispersed (0.2  $\mu\text{M}$ ) in fresh water; (e) anhydrous state TEM image drop-deposited on a nickel grid; (f) SEM image of the as-synthesized OCN samples (gold/palladium coated); (g) AFM image and (h) particle height distribution ( $H_{av}$ ) from AFM.

PEG<sub>400</sub>-coated OCN particles exhibited a diameter (number-averaged) of  $7 \pm 3$  nm and  $8 \pm 2$  nm respectively (Fig. 1(d)). The polydispersity and zeta potential of particles were measured as  $0.08 \pm 0.03$  and  $-8 \pm 3$  mV, respectively.

Anhydrous state diameters were also obtained from TEM measurements. As shown in Fig. 1(e), the as-synthesized OCN were well dispersed in narrow distributions with diameter  $9 \pm 3$  nm. The observed morphological clustering was primarily due to the hydrogen bonding interactions among adjacent nanoparticles through the pendant hydroxyl end-groups of the PEG-passivated OCN. Scanning electron microscopy (SEM) images also confirmed that these particles are spherical (Fig. 1(f)). AFM shows that as-synthesized OCN particles have a particle height ( $H_{av}$ ) of  $11 \pm 3$  nm

(Figs. 1(g) and 1(h)). The discrepancy between the particle diameter and the height values can be explained due to the high tendency of these particles for aggregation on a solid surface. It was difficult to find significant amount of isolated OCN, a problem that was also encountered by previous investigators [33–35].

FT-IR spectra displayed the expected characteristic stretching and vibration bands i.e., C–O–C, C–OH, and C–H bonds (Fig. 2(a)). Stretching vibrations of carbonyl (C=O;  $\sim 1,620$   $\text{cm}^{-1}$ ) and symmetric/asymmetric stretching vibrations of carboxylate groups ( $\sim 1,200$ – $1,300$   $\text{cm}^{-1}$ ) were also identified in low intensities, presumably due to the oxidation/decomposition of C–OH bonds by the residual air or under the microwave conditions. However,  $^1\text{H}$  NMR spectra of OCN (coated with PEG<sub>400</sub>) confirmed that the organic

coating predominantly retained its structural integrity after microwave processing (Fig. S2 (in the ESM)). Energy dispersive X-ray (EDX) spectra were recorded both in dry- (Fig. 2(b)) and wet- (Fig. 2(c)) dispersed states. The EDX spectra (Fig. 2(d)) indicated that in both wet and dry dispersed states, the fluorescent fractions contained mainly carbon (dry dispersed: C = 87%, O = 9%; wet dispersed: C = 81%, O = 12%) with insignificant amounts of impurities detected. Raman spectroscopy of OCN samples showed the presence of characteristic peaks at  $\sim 1,580\text{ cm}^{-1}$  characteristic of the in-plane stretching vibration mode  $E_{2g}$  of single-crystal graphite

(G band) (Fig. 2(e)). A prominent defect band (D) around  $1,350\text{ cm}^{-1}$  also originates from a hybridized vibrational mode associated with graphene edges and it indicates the presence of some disorder in the graphene structure. UV–vis spectroscopy showed a broad absorbance in the region of 250–800 nm and a peak at  $\sim 280\text{ nm}$ , which is ascribed to the  $n\text{-}\pi^*$  transition of the C=O band and the  $\pi\text{-}\pi^*$  transition of the conjugated C=C band, indicating the presence of carbon nanoparticles (Fig. 2(f)).

To evaluate the stability of these particles under physiological condition, a “blood smear” assay was

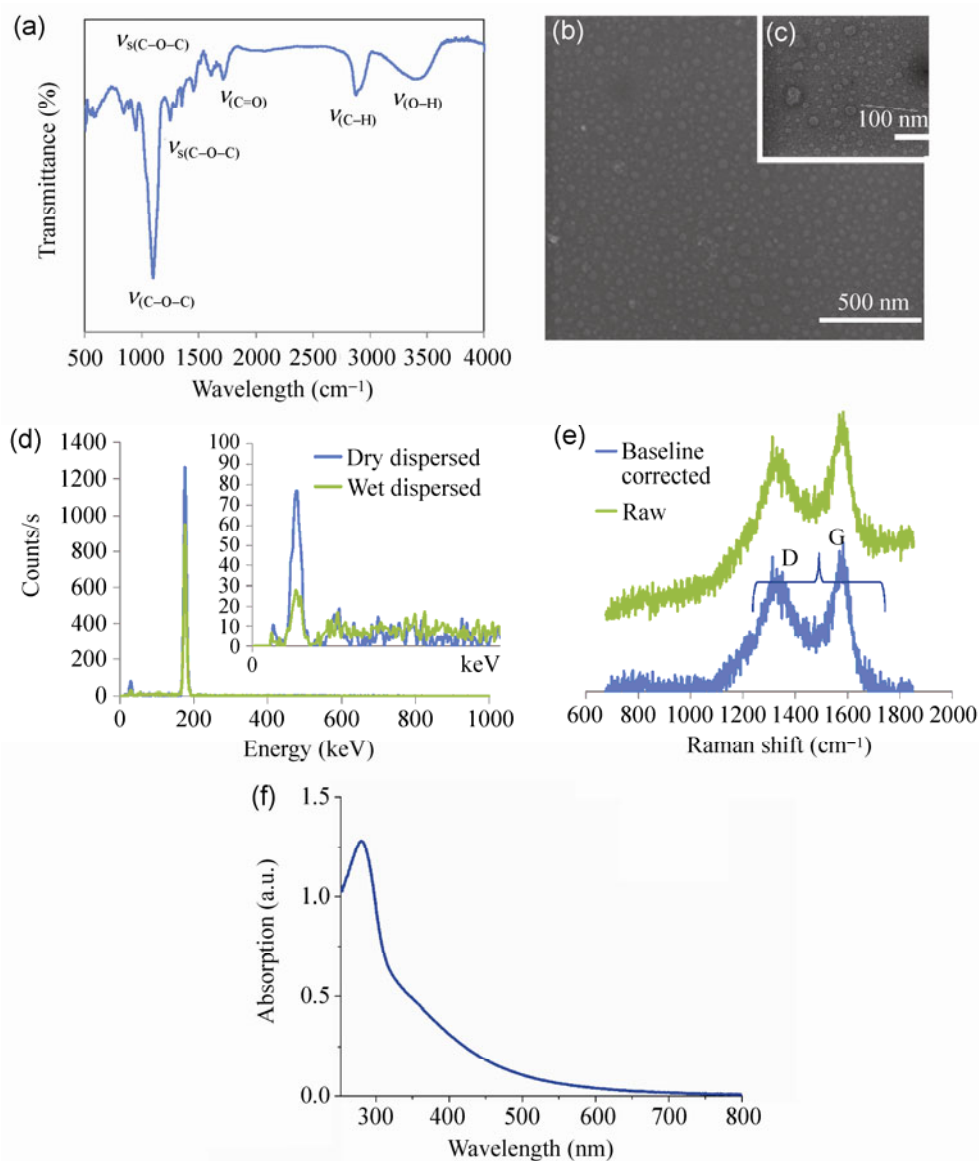


**Figure 2** (a) FT–IR spectroscopy signals of as-synthesized OCN; SEM images in dry- (b) and wet-dispersed state (c); (d) EDX spectra; (e) Raman spectra of OCN raw (green) and baseline corrected (blue); (f) UV–vis absorption spectrum of OCN.

performed. Morphological changes in lymphocytes and blood clumping was monitored using conventional light microscopy under a high-power field. As shown in Figs. 3(a) and 3(b), no comprehensive clumping or morphological alterations were noticed in rodent blood treated with OCN (blood:OCN = 4:1). To assess the stability of OCN under a biological environment *in vitro*, OCN was incubated with rabbit plasma (OCN:plasma = 1:100) for 30 min and the integrity of the particles was observed by dynamic light scattering measurements. Very negligible changes in particle diameters were noticed when incubated with rabbit plasma. The particle diameter before and after incubation with plasma was found to be  $12 \pm 3$  nm and  $9 \pm 2$  nm respectively, which indicates the high stability of OCN in a plasma environment.

Due to the high concentration of hemoglobin (12 to 15 g/dL), inherently blood has a strong optical absorption, which allows the visualization of blood vessels by PAI. Since hemoglobin is a dominant optical absorber in humans and generates strong PA signals, it is important to get a relative estimate of the optical absorption of the exogenous contrast agent with hemoglobin.

We compared the PA efficacy of OCN with blood at various excitation wavelengths. Figure 3(a) shows the

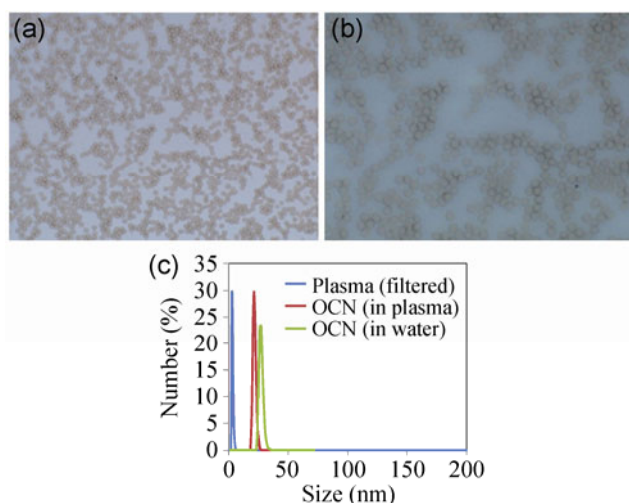


**Figure 3** Optical micrograph of rodent serum from a “blood smear” experiment: (a) Untreated (magnification: 20x) and (b) treated with OCN at a 4:1 ratio (magnification: 40x; serum:OCN); (c) *in vitro* stability of OCN in a biological environment (rabbit plasma) observed by the changes in dynamic light scattering and showing no tendency to aggregation.

PA signals obtained from a tygon tube (I.D. 510  $\mu$ m) filled with OCN (33 vol.%) and rat whole blood (hematocrit ~45%; hemoglobin ~15 g/dL). The tygon tube is transparent; therefore, it does not absorb enough light to produce any measurable PA signal. With the laser tuned to an excitation wavelength of 670 nm, OCN (33 vol.%) exhibited 9.4 times PA signal enhancement compared with the rat blood (Fig. 4(a)).

Figure 4(b) shows the PA spectra (peak-to-peak PA signal amplitude in log scale versus excitation light wavelength) of the OCN (33 vol.%, in black) and the rat blood (in red). The excitation wavelength range was 450–850 nm, excluding the range of 685–730 nm due to the gap between two lasers. The PA signal obtained from OCN was much stronger than, or comparable with, that from blood over the broad wavelength range, which covered both visible and NIR radiation. Over the 605–760 nm wavelength range, the PA signal from OCN was five times stronger than that from blood and over the 635–670 nm window the PA signal from OCN was nine times stronger. The NIR window is well known and suitable for deep PA imaging *in vivo* due to weak hemoglobin absorption within this window. Figure 4(c) shows how the PA signal amplitude changes for several laser wavelengths from serially diluted OCN. The data show an approximately linear relationship between the PA signal amplitude and the concentration of OCN. In comparison with the rat blood, OCN exhibited 14.2 times and 3.5 times PA signal enhancement (660 nm) at concentrations of 33 vol.% and 11 vol.%, respectively. A measurable PA signal could not be generated from 0.4 vol.% OCN at a wavelength of 660 nm, presumably due to the low absorption under these conditions. However, significant PA signals still could be produced even at such a low concentration at other wavelengths. The PA signal amplitude and the concentration of OCN follow a linear relationship as shown in Fig. 4(d). This preliminary spectroscopic study confirms that the high sensitivity makes OCN an excellent candidate for PAI applications.

The detection of axillary lymph nodes through real-time PA guidance of SLN biopsy could minimize resection time by providing precise spatial localization of the SLN, which is poorly achieved with current optical and nuclear techniques. Figure 5(h) shows a

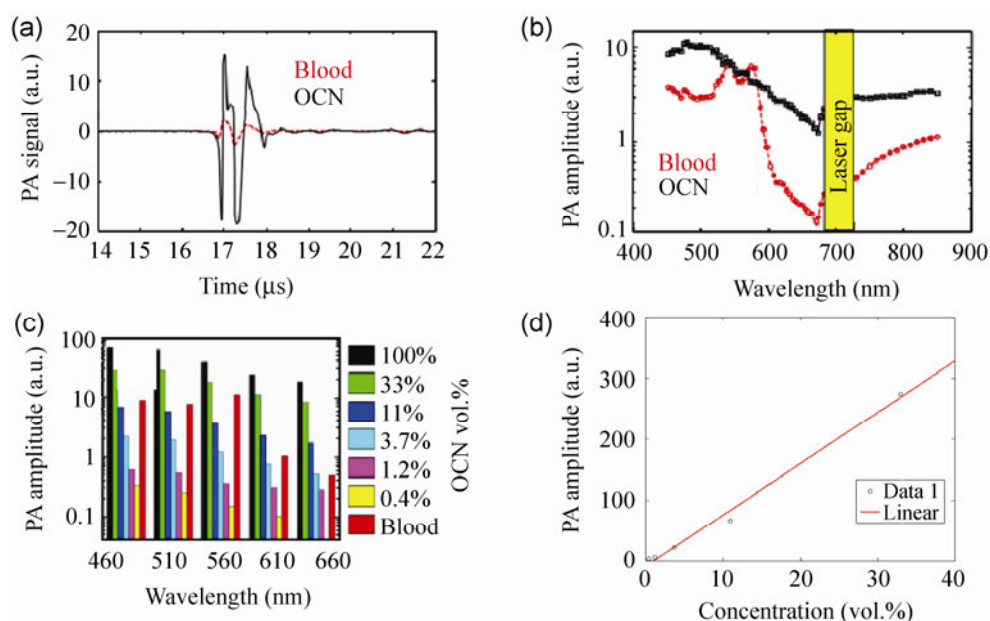


**Figure 4** (a) PA spectroscopy signals were generated from two tygon tubes (I.D. 510  $\mu\text{m}$ ) filled with OCN (33 vol.%) and rat blood, respectively. The laser was tuned to a wavelength of 670 nm. (b) PA spectra of OCN (33 vol.%) and rat blood in log scale over a 450–850 nm wavelength range, with a laser gap between 685–730 nm. (c) PA signal of serially diluted OCN at various wavelengths. (d) Representative plot showing a linear relationship between the PA signal amplitude and the concentration at 510 nm ( $R^2 = 0.987$ ).

representative digital photograph of a nude mouse acquired prior to image acquisition. Before the OCN nanoparticle injection, a PA control image was obtained, which is shown in the form of a maximum intensity projection (MAP) in Fig. 5(a). The vasculature in close proximity of an axial node (marked as BV) is clearly seen, with a resolution of  $\sim 80 \mu\text{m}$ . The intrinsic optical absorption of Lymph node (LN) was negligible without PA contrast and therefore they were not visible. Following intradermal OCN injection (in nanopure water, 0.2  $\mu\text{M}$ ) in the left forepaw of the mouse, the PA image MAP of the same area was acquired dynamically for 210 min. Within 2 min post-injection of OCN, a lymph node (Fig. 5(b)) was clearly visible with up to  $\sim 51$  times contrast enhancement. The lymph node was monitored further over time, with declining contrast enhancement of the draining lymph node observed over 210 min (Figs. 5(c)–5(f)). Figure 5(f) is the post-injection PA image of the same region 210 min after the OCN injection, indicating much weaker contrast and plausible clearance of the particles from LN. Figure 5(i) depicts the same mouse with the skin removed after the completion of the PA imaging. The

appearance and absence of dark-colored deposition in the optical images of excised lymph nodes from OCN-injected (Fig. 5(j)) and saline-injected (Fig. 5(k)) mouse respectively confirmed that the desired signal is a consequence of the OCN accumulation. The relatively smaller diameter of OCN results in its faster clearance, and therefore an obvious decay in PA signal sensitivity was observed after 210 min. The PA system for *in vivo* experiments achieves  $\sim 15 \mu\text{m}$  axial resolution,  $\sim 45 \mu\text{m}$  lateral resolution, 3 mm penetration depth and 1 min temporal resolution for a 3D image.

*In vivo* PA imaging was performed non-invasively on a nude mouse femoral vessel to assess the preliminary clearance profile and vessel imaging of OCN. The laser was tuned to a wavelength of 650 nm. PA images of the femoral vessels were taken with intervals of 1–2 min after OCN (25 vol.%, 100  $\mu\text{L}$ ) was intravenously injected through the tail vein. A series of PA MAP images of the femoral area are presented in Figs. 6(a)–6(e), where the color bars are identical. The vasculature was imaged with a high contrast-to-noise ratio (CNR = 10) and high spatial resolution of about 80  $\mu\text{m}$ . Figure 6(a) shows the PA image before

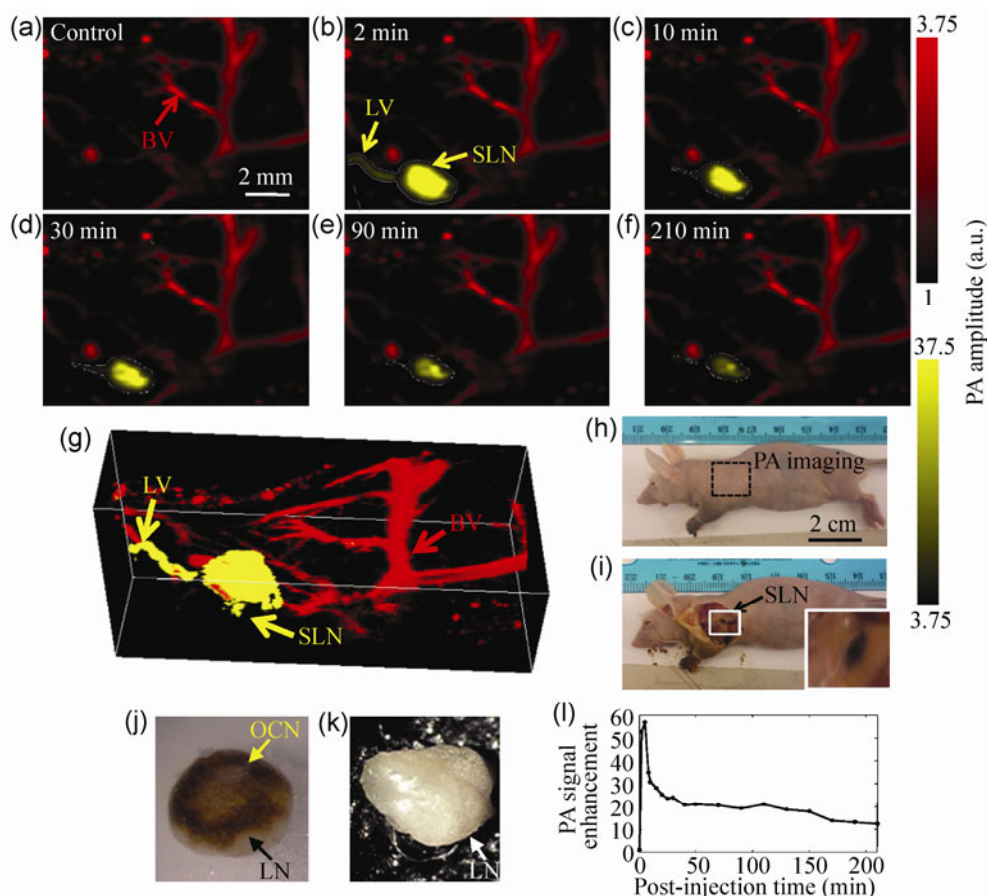


**Figure 5** Non-invasive real-time *in vivo* PA imaging of SLN in a nude mouse: For all PA images, the laser was tuned to a wavelength of 650 nm. (a) Control PA image acquired before OCN injection. Red parts represent optical absorption from blood vessels (BV); (b) PA image acquired immediately (2 min) after the OCN injection. Blood vessel (BV), lymph vessel (LV) and sentinel lymph node (SLN) are marked with arrows, and the SLN is visible in (b)–(e), however, the contrast is much weaker after 210 min post-injection in (f). (g) 3D depiction of the SLN and BVs immediately after OCN injection, (h) Photograph of the nude mouse before taking the PA images. The scanning region is marked with a black dotted square. (i) Photograph of the mouse with the skin removed after PA imaging, accumulation of dark-colored OCN particles are visible in lymph nodes; (j) excised and isolated lymph node from mouse injected with OCN after 0.5 h and (k) injected with saline; (l) PA signal enhancement in the SLN after the injection of OCN nanoparticle as a function of post-injection time. For (a)–(d): FOV = 12 mm × 10 mm, step size along the x-direction = 40 μm, step size along the y-direction = 100 μm, raster scanning for a 3D image = ~1 min, B-scan frame rate = ~1.5 Hz, total scan time = ~210 min. No signal averaging was used.

OCN injection. Figures 6(b)–6(e) show PA images obtained at 1 (b), 6 (c), 15 (d), and 30 min (e) post-injection of OCN. With the administration of the exogenous contrast agent, OCN in water (0.2 μM), the optical absorption of the blood was increased and the contrast between the vessels and the background tissues was enhanced. Thus, in Figs. 6(b)–6(e), the vasculature is seen with greater clarity in comparison to Fig. 6(a). Figure 6(e) was acquired at 30 min post-injection of OCN. Due to the rapid clearance of the OCN from the blood, the optical absorption in the

blood vessels decreased significantly. The differential image in Fig. 6(f) is a result of the subtraction of the pre-injection image in Fig. 6(a) from the post-injection image in Fig. 6(c). This image depicts the distribution of differential optical absorption in the vasculature induced by the exogenous contrast agent. The injection of saline alone was not found to make any distinctive changes in PA signals, which also agrees with our findings reported previously [6]. The clearance of OCN from a typical femoral blood vessel (marked by a dashed-square in Fig. 6(a)) is quantified in Fig. 6(g). OCN

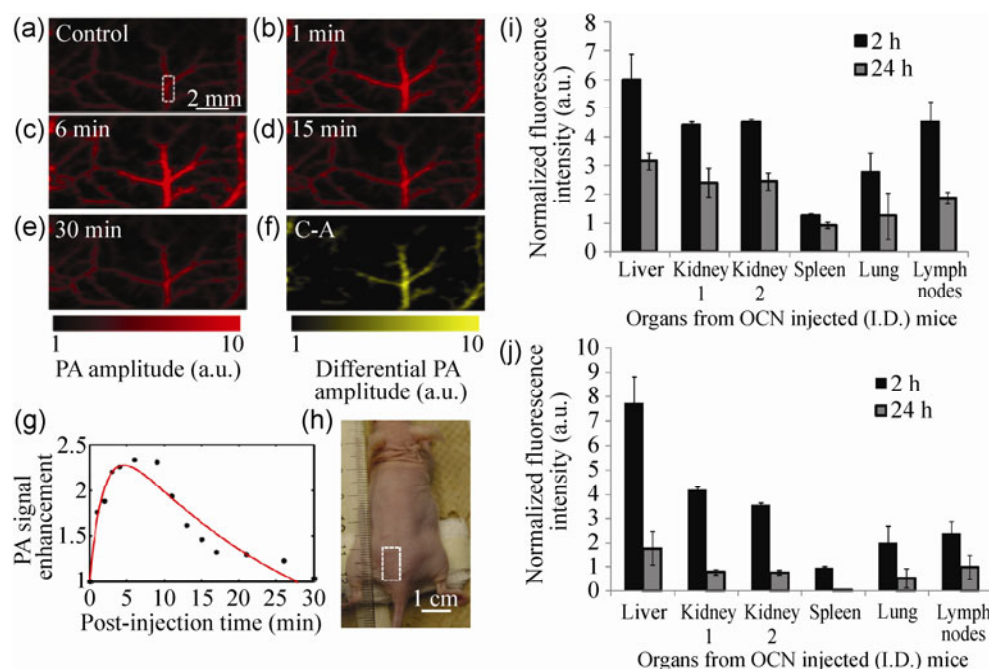


**Figure 6** Noninvasive PA imaging of femoral vasculature of a nude mouse employing OCN as contrast agent. The PA signal from the femoral vessels was monitored after OCN (25 vol.%, 100  $\mu$ L) was intravenously injected slowly through the tail vein. The laser was tuned to a wavelength of 650 nm. (a) PA MAP image acquired before the injection of OCN. Red parts represent optical absorption from blood vessels. (b)–(e) PA MAP images obtained at 1 (b), 6 (c), 15 (d), and 30 min (e) post-injection of OCN. Red scale bar corresponds to (a)–(e); (f) Differential image that was obtained by subtracting the pre-injection image from the post-injection image (Image f = Image e – Image a); (g) clearance of OCN from a typical femoral blood vessel, marked by a dashed-square in (a). Time 0 is the time point of injection. The maximum enhanced contrast is 2.3 at 6 min post-injection. Red curve: Exponential fit ( $2.9 \cdot \exp(-0.04 \cdot x) + (-1.9) \cdot \exp(-0.5 \cdot x)$ ,  $R^2 = 0.92$ ); (h) Optical photograph of a nude mouse showing the area of imaging; *In vivo* biodistribution of OCN nanoparticles: Organ distribution of the nanoparticles based on normalized fluorescent intensities in major organs 2 h (black bars) and 24 h (grey bars) after intradermal (i) and intravenous (j) injection of particles.

particles maintained a clear distribution phase followed by a clearance phase to give a biexponential decay of the PA signal in blood, similar to reports with other nanoparticles [4]. At 6 min post-injection, the signal amplitude of the blood vessels was increased 230% compared to that in the control blood vessels. It should be pointed out that the clearance of OCN takes only ~30 min, much faster than that of other previously reported nanoparticles, which usually takes several hours [43].

The preliminary biodistribution of OCN was conducted in mice to study the nanoparticle accumulation in different organs. Two modes of administration were followed to corroborate with the real-time lymph node imaging (I.D.) and blood vessel imaging (I.V.). Nanoparticles were injected intradermally and intravenously (1 mL/kg) to mice ( $n = 5$ ) and the

major organs were collected at 2 h and 24 h post-administration. For both these cases, liver was the predominant organ for OCN accumulation (Figs. 6(i) and 6(j)). The other major sites of accumulation were kidney, lymph nodes and spleen. Although more in depth *in vivo* studies are warranted, our initial results show that OCN presumably take reticuloendothelial (RES) systemic routes for their clearance. Interestingly, accumulation in the lung was observed with both intradermal and intravenously injected particles. The filtration through the lung tissue, which is the first capillary bed OCN encounter upon injection, is presumably responsible for OCN aggregation in the lung. At 24 h, the level of signal intensity decreased about four fold in the major organs by intravenous injection, which correlates with the rapid clearance *in vivo*. The corresponding collection values of signals from

intradermally injected mice decreased approximately two times, indicating a slower mechanism of clearance for OCN by this route.

## 4 Conclusions

We report a simple and commercially amenable “green syntheses” of carbon nanoparticles. These particles are markedly smaller than the previously reported particles (gold, SWNT, copper, etc.) used for PA SLN imaging, which was manifested in rapid particle relocation from the paw to the axillary node. The exceptionally rapid signal enhancement of the SLN suggests that flexible, real-time intraoperative use rather than the typical perioperative patient procedure may be possible. The lymphatic transport behavior of the nanoparticles is highly dependent on their sizes and shapes. Due to their larger sizes (SWNT, gold, etc.) and non-spherical shapes (gold nanorods and SWNTs) or even the lack of temporal resolution of the PA system (~24 min for a 3D image), none of the previously reported agents have shown such facile lymphatic transport as achieved in this work. Our approach offers greater convenience and reduced procedural expense, as well as improved surgical advantage, given the ability to directly and rapidly recognize the depth and orientation of the nodes with intraoperative photoacoustic tomography (PAT) as the patient is positioned on the table for easier resection. In contrast, the current most sensitive techniques with radiolabeled colloids provide only low lateral plane resolution to guide the site of incision, and limited vertical resolution to anticipate the depth of dissection required. We envision that rather than being permanently entrapped or phagocytosed within the lymph nodes, the tiny NIR particles may retain their structural integrity and migrate out into the lymphatic chain and into the circulation system via the thoracic duct.

## Acknowledgements

The financial support from the American Heart Association (AHA) Nos. 0835426N and 11IRG5690011 and National Institutes of Health (NIH) under the Grants Nos. NS059302, CA119342, R01 EB000712, R01 EB008085, R01 CA134539, and U54 Nos. CA136398

and HL073646 and the National Cancer Institute (NCI) under the Grant No. N01CO37007 is greatly appreciated. L.W. and B.S. appreciate the financial support of National Natural Science Foundation of China (Nos. 81101087, 81130028, and 31210103913), China Scholarship Council (No. 2011823056), Science and Technology Research Project of Heilongjiang Education Department (No. 12511325), China Postdoctoral Science Foundation (No. 2012M510992) and Heilongjiang Postdoctoral Foundation (No. LBH-Z11054), TEM, SEM, and AFM were conducted at the Nano Research Facility, a member of National Nanotechnology Infrastructure Network-National Science Foundation (NNIN-NSF) under Grant No. ECS-0335765.

**Electronic Supplementary Material:** Supplementary material (schematic of the PA system and  $^1\text{H}$  NMR spectra of  $\text{PEG}_{400}$  and OCN) is available in the online version of this article at <http://dx.doi.org/10.1007/s12274-013-0308-8>.

## References

- [1] Wang, X. D.; Pang, Y. J.; Ku, G.; Xie, X. Y.; Stoica, G.; Wang, L. V. Noninvasive laser-induced photoacoustic tomography for structural and functional *in vivo* imaging of the brain. *Nat. Biotechnol.* **2003**, *21*, 803–806.
- [2] Jokerst, J. V.; Thangaraj, M.; Kempen, P. J.; Sinclair, R.; Gambhir, S. S. Photoacoustic imaging of mesenchymal stem cells in living mice via silica-coated gold nanorods. *ACS Nano.* **2012**, *6*, 5920–5930.
- [3] Wang, L. V.; Hu, S. Photoacoustic tomography: *In vivo* imaging from organelles to organs. *Science* **2012**, *335*, 1458–1462.
- [4] Pan, D.; Pramanik, M.; Wickline, S. A.; Wang, L. V.; Lanza, G. M. Recent advances in colloidal gold nanobeacons for molecular photoacoustic imaging. *Contrast Media Mol. Imaging* **2011**, *6*, 378–388.
- [5] Chen, Z. Y.; Ma, L. J.; Liu, Y.; Chen, C. Y. Applications of functionalized fullerenes in tumor theranostics. *Theranostics* **2012**, *2*, 238–250.
- [6] de la Zerde, A.; Liu, Z.; Bodapati, S.; Teed, R.; Vaithilingam, S.; Khuri-Yakub, B. T.; Chen, X. Y.; Dai, H. J.; Gambhir, S. S. Ultrahigh sensitivity carbon nanotube agents for photoacoustic molecular imaging in living mice. *Nano Lett.* **2010**, *10*, 2168–72.
- [7] Li, M. L.; Oh, J. T.; Xie, X.; Ku, G.; Wang, W.; Li, C.; Lungu, G.; Stoica, G.; Wang, L. V. Simultaneous molecular

- and hypoxia imaging of brain tumors *in vivo* using spectroscopic photoacoustic tomography. *Proc. IEEE* **2008**, *96*, 481–489.
- [8] Wang, X. D.; Xie, X. Y.; Ku, G.; Wang, L. V.; Stoica, G. Noninvasive imaging of hemoglobin concentration and oxygenation in the rat brain using high-resolution photoacoustic tomography. *J. Biomed. Opt.* **2006**, *11*, 024015.
- [9] Pan, D.; Pramanik, M.; Senpan, A.; Allen, J. S.; Zhang, H. Y.; Wickline, S. A.; Wang, L. V.; Lanza, G. M. Molecular photoacoustic imaging of angiogenesis with integrin-targeted gold nanobeacons. *FASEB J.* **2011**, *25*, 875–882.
- [10] Pan, D.; Pramanik, M.; Senpan, A.; Ghosh, S.; Wickline, S. A.; Wang, L. V.; Lanza, G. M. Near infrared photoacoustic detection of sentinel lymph nodes with gold nanobeacons. *Biomaterials* **2010**, *31*, 4088–4093.
- [11] Schneider, B. P.; Miller, K. D. Angiogenesis of breast cancer. *J. Clin. Oncol.* **2005**, *23*, 1782–1790.
- [12] Agarwal, A.; Huang, S. W.; O'Donnell, M.; Day, K. C.; Day, M.; Kotov, N. A.; Ashkenazi, S. Targeted gold nanorod contrast agent for prostate cancer detection by photoacoustic imaging. *J. Appl. Phys.* **2007**, *102*, 064701.
- [13] de la Zerda, A.; Zavaleta, C.; Keren, S.; Vaithilingam, S.; Bodapati, S.; Liu, Z.; Levi, J.; Smith, B. R.; Ma, T. J.; Oralkan, O.; Cheng, Z.; Chen, X. Y.; Dai, H. J.; Khuri-Yakub, B. T.; Gambhir, S. S. Carbon nanotubes as photoacoustic molecular imaging agents in living mice. *Nat. Nanotechnol.* **2008**, *3*, 557–562.
- [14] Pan, D.; Cai, X.; Yalaz, C.; Senpan, A.; Omanakuttan, K.; Wickline, S. A.; Wang, L. V.; Lanza, G. M. Photoacoustic sentinel lymph node imaging with self-assembled copper neodecanoate nanoparticles. *ACS Nano* **2012**, *6*, 1260–1267.
- [15] Jose, J.; Grootendorst, D. J.; Vijn, T. W.; Wouters, M. W.; van Boven, H.; van Leeuwen, T. G.; Steenbergen, W.; Ruers, T. J. M.; Manohar, S. Initial results of imaging melanoma metastasis in resected human lymph nodes using photoacoustic computed tomography. *J. Biomed. Opt.* **2011**, *16*, 096021.
- [16] Purushotham, A. D.; Upponi, S.; Klevesath, M. B.; Bobrow, L.; Millar, K.; Myles, J. P.; Duffy, S. W. Morbidity after sentinel lymph node biopsy in primary breast cancer: Results from a randomized controlled trial. *J. Clin. Oncol.* **2005**, *23*, 4312–4321.
- [17] Krag, D. N.; Anderson, S. J.; Julian, T. B.; Brown, A. M.; Harlow, S. P.; Costantino, J. P.; Ashikaga, T.; Weaver, D. L.; Mamounas, E. P.; Jalovec, L. M. et al. Sentinel-lymph-node resection compared with conventional axillary-lymph-node dissection in clinically node-negative patients with breast cancer: Overall survival findings from the NSABP B-32 randomised phase 3 trial. *Lancet Oncol.* **2010**, *11*, 927–933.
- [18] Krag, D.; Weaver, D.; Ashikaga, T.; Moffat, F.; Klimberg, V. S.; Shriver, C.; Feldman, S.; Kusminsky, R.; Gadd, M.; Kuhn, J. et al. The sentinel node in breast cancer—A multicenter validation study. *N. Eng. J. Med.* **1998**, *339*, 941–946.
- [19] McMasters, K. M.; Tuttle, T. M.; Carlson, D. J. Sentinel lymph node biopsy for breast cancer: A suitable alternative to routine axillary dissection in multi-institutional practice when optimal technique is used. *J. Clin. Oncol.* **2000**, *18*, 2560–2566.
- [20] Zhang, H. F.; Maslov, K.; Stoica, G.; Wang, L. V. Functional photoacoustic microscopy for high-resolution and noninvasive *in vivo* imaging. *Nat. Biotechnol.* **2006**, *24*, 848–851.
- [21] Song, K. H.; Stein, E. W.; Margenthaler, J. A.; Wang, L. V. Noninvasive photoacoustic identification of sentinel lymph nodes containing methylene blue *in vivo* in a rat model. *J. Biomed. Opt.* **2008**, *13*, 054033.
- [22] Li, P. C.; Wang, C. R. C.; Shieh, D. B.; Wei, C. W.; Liao, C. K.; Poe, C.; Jhan, S.; Ding, A. A.; Wu, Y. N. *In vivo* photoacoustic molecular imaging with simultaneous multiple selective targeting using antibody-conjugated gold nanorods. *Opt. Express* **2008**, *16*, 18605–18615.
- [23] Wang, Z. J.; Wu, L. N.; Cai, W. Size-tunable synthesis of monodisperse water-soluble gold nanoparticles with high X-ray attenuation. *Chem. Eur. J.* **2010**, *16*, 1459–1463.
- [24] Pramanik, M.; Swierczewska, M.; Green, D.; Sitharaman, V.; Wang, L. V. Single-walled carbon nanotubes as a multimodal-thermoacoustic and photoacoustic-contrast agent. *J. Biomed. Opt.* **2009**, *14*, 034018.
- [25] de la Zerda, A.; Bodapati, S.; Teed, R.; May, S. Y.; Tabakman, S. M.; Liu, Z.; Khuri-Yakub, B. T.; Chen, X. Y.; Dai, H. J.; Gambhir, S. S. Family of enhanced photoacoustic imaging agents for high-sensitivity and multiplexing studies in living mice. *ACS Nano* **2012**, *6*, 4694–4701.
- [26] Hu, Z. Y.; Pantoş, G. D.; Kuganathan, N.; Arrowsmith, R. L.; Jacobs, R. M. J.; Kociok-Köhn, G.; O'Byrne, J.; Jurkschat, K.; Burgos, P.; Tyrrell, R. M. et al. Interactions between amino acid-tagged naphthalenediimide and single walled carbon nanotubes for the design and construction of new bioimaging probes. *Adv. Funct. Mater.* **2012**, *22*, 503–518.
- [27] Liu, Z.; Tabakman, S. M.; Chen, Z.; Dai, H. J. Preparation of carbon nanotube bioconjugates for biomedical applications. *Nature Protoc.* **2009**, *4*, 1372–1381.
- [28] Sohrabnezhad, S.; Pourahmad, A.; Sadjadi, M. A. New methylene blue incorporated in mordenite zeolite as humidity sensor material. *Mater. Lett.* **2007**, *61*, 2311–2314.
- [29] Xie, J.; Lee, S.; Chen, S. Y. Nanoparticle-based theranostic agents. *Adv. Drug Deliv. Rev.* **2010**, *62*, 1064–1079.
- [30] Brewer, G. J. Copper toxicity in the general population. *Clin. Neurophysiol.* **2010**, *121*, 459–460.

- [31] Schipper, M. L.; Nakayama-Ratchford, N.; Davis, C. R.; Kam, N. W. S.; Chu, P.; Liu, Z.; Sun, X. M.; Dai, H. J.; Gambhir, S. S. A pilot toxicology study of single-walled carbon nanotubes in a small sample of mice. *Nat Nanotechnol.* **2008**, *3*, 216–221.
- [32] Yang, S. T.; Luo, J. B.; Zhou, Q. H.; Wang, H. F. Pharmacokinetics, metabolism and toxicity of carbon nanotubes for biomedical purposes. *Theranostics* **2012**, *2*, 271–282.
- [33] Pan, D.; Cai, X.; Kim, B.; Stacy, A. J.; Wang, L. V.; Lanza, G. M. Rapid synthesis of near infrared polymeric micelles for real-time sentinel lymph node imaging. *Adv. Healthcare Mater.* **2012**, *1*, 582–589.
- [34] Sun, Y. P.; Zhou, B.; Lin, Y.; Wang, W.; Fernando, K. A.; Pathak, P.; Meziani, M. J.; Harruff, B. A.; Wang, X.; Wang, H. F. et al. Quantum-sized carbon dots for bright and colorful photoluminescence. *J. Am. Chem. Soc.* **2006**, *128*, 7756–7757.
- [35] Liu, H. P.; Ye, T.; Mao, C. D. Fluorescent carbon nanoparticles derived from candle soot. *Angew. Chem., Int. Ed.* **2007**, *46*, 6473–6475.
- [36] Bourlinos, A. B.; Stassinopoulos, A.; Anglos, D.; Zboril, R.; Georgakilas, V.; Giannelis, E. P. Photoluminescent carbogenic dots. *Chem. Mater.* **2008**, *20*, 4539–4541.
- [37] Huang, P.; Lin, J.; Wang, X. S.; Wang, Z.; Zhang, C. L.; He, M.; Wang, K.; Chen, F.; Li, Z. M.; Shen, G. X. et al. Light-triggered theranostics based on photosensitizer-conjugated carbon dots for simultaneous enhanced-fluorescence imaging and photodynamic therapy. *Adv. Mater.* **2012**, *37*, 5104–5110.
- [38] Liu, Z.; Liang, X. J. Nano-carbons as theranostics. *Theranostics* **2012**, *2*, 235–237.
- [39] Cao, L.; Yang, S. T.; Wang, X.; Luo, P. G.; Liu, J. H.; Sahu, S.; Liu, Y. M.; Sun, Y. P. Competitive performance of carbon “quantum” dots in optical bioimaging. *Theranostics* **2012**, *2*, 295–301.
- [40] Swierczewska, M.; Choi, K. Y.; Mertz, E. L.; Huang, X. L.; Zhang, F.; Zhu, L.; Yoon, H. Y.; Park, J. H.; Bhirde, A.; Lee, S. et al. A facile, one-step nanocarbon functionalization for biomedical applications. *Nano Lett.* **2012**, *12*, 3613–3620.
- [41] Zhu, Y.; Li, J.; Li, W. X.; Zhang, Y.; Yang, X. F.; Chen, N.; Sun, Y. H.; Zhao, Y.; Fan, C. H.; Huang, Q. The biocompatibility of nanodiamonds and their application in drug delivery systems. *Theranostics* **2012**, *2*, 302–312.
- [42] Liu, Z.; Robinson, J. T.; Tabakman, S. M.; Yang, K.; Dai, H. J. Carbon materials for drug delivery and cancer therapy. *Mater. Today* **2011**, *14*, 316–323.
- [43] Zhou, C.; Hao, G. Y.; Thomas, P.; Liu, J. B.; Yu, M. X.; Sun, S. S.; Öz, O. K.; Sun, X. K.; Zheng, J. Near infrared emitting radioactive gold nanoparticles with small-molecule-like pharmacokinetics. *Angew. Chem., Int. Ed.* **2012**, *51*, 10118–10122.